REPORT DOCUMENTATION PAGE

Public reporting burden for this collection of information is estimated to average 1 hour per response, including the time for reviewing instructions, searching existing data sources, gathering and maintaining the data needed, and completing and reviewing this collection of information. Send comments regarding this burden estimate or any other aspect of this collection of information, including suggestions for reducing this burden to Department of Defense, Washington Headquarters Services, Directorate for Information Operations and Reports (0704-0188), 1215 Jefferson Davis Highway, Suite 1204, Arlington, VA 22202-4302. Respondents should be aware that notwithstanding any other provision of law, no person shall be subject to any penalty for failing to comply with a collection of information if it does not display a currently valid OMB control number. **PLEASE DO NOT RETURN YOUR FORM TO THE ABOVE ADDRESS.**

1. REPORT DATE (DD-MM-YYYY)	2. REPORT TYPE	3. DATES COVERED (From - To)
May 2006	Conference Paper POSTPRINT	2005 - 2006

4. TITLE AND SUBTITLE	5a. CONTRACT NUMBER
Deployment Repeatability Testing of Composite Tape Springs for Space Optics Applications	
	5b. GRANT NUMBER
	5c. PROGRAM ELEMENT NUMBER

6. AUTHOR(S)
Jonathan T. Black, Jeffrey A. Whetzal,* Brett J. deBlonk,[†] Jack J Massarello[†]

5d. PROJECT NUMBER
5e. TASK NUMBER
5f. WORK UNIT NUMBER

7. PERFORMING ORGANIZATION NAME(S) AND ADDRESS(ES) AND ADDRESS(ES)	8. PERFORMING ORGANIZATION REPORT NUMBER
University of Kentucky *South Dakota School of Mines & Lexington, KY 40506 Technology Rapid City, SD 57701	

9. SPONSORING / MONITORING AGENCY NAME(S) AND ADDRESS(ES)	10. SPONSOR/MONITOR'S ACRONYM(S)
†Air Force Research Laboratory Space Vehicles 3550 Aberdeen Ave SE Kirtland AFB, NM 87117-5776	
	11. SPONSOR/MONITOR'S REPORT NUMBER(S)
	AFRL-VS-PS-TP-2006-1017

12. DISTRIBUTION / AVAILABILITY STATEMENT

Approved for public release; distribution is unlimited. (Clearance #VS06-0114)

14. ABSTRACT
Tape springs are of interest to the space structures community because of their high packaging ratios, ability to self-deploy, and high stiffness-to-mass ratios. The current drive to lightweight telescopes has focused mostly on decreasing the mass of the mirrors, yet decreasing the mass of the support structure may also generate significant mass savings. Here the use of carbon-fiber-composite tape springs is examined as a potential support structure of a secondary mirror in a Cassegrain-type telescope configuration. For the tape springs to be useful in this capacity, they must exhibit deployment precision to levels consistent with optical control systems. Deployment repeatability of such structures is investigated through simplified sensing configurations that include a linear structural element and a tripod comprised of carbon-fiber-composite tape springs supporting a simulated secondary mirror. Single tape springs showed deployment repeatability on the order of 100 microns, while the tripod configuration showed deployment repeatability on the order of 50 microns.

15. SUBJECT TERMS
Tape Springs, Space Optics, Mirror, Space Structures, Lightweight Telescopes, Support Structure, Carbon-Fiber-Composite Tape Springs, Space Vehicles

16. SECURITY CLASSIFICATION OF:			17. LIMITATION OF ABSTRACT	18. NUMBER OF PAGES	19a. NAME OF RESPONSIBLE PERSON
a. REPORT	**b. ABSTRACT**	**c. THIS PAGE**	Unlimited	15	Jack J. Massarello
Unclassified	Unclassified	Unclassified			**19b. TELEPHONE NUMBER** (include area code) 505-853-5383

47th AIAA/ASME/ASCE/AHS/ASC Structures, Structural Dynamics, and Materials Confere
1 - 4 May 2006, Newport, Rhode Island

AIAA 2006-1905

Deployment Repeatability Testing of Composite Tape Springs for Space Optics Applications

Jonathan T. Black[*]
University of Kentucky, Lexington, KY 40506

Jeffrey A. Whetzal[†]
South Dakota School of Mines and Technology, Rapid City, SD 57701

Brett J. deBlonk[‡] and Jack J. Massarello[§]
Air Force Research Laboratory Space Vehicles Directorate, Albuquerque, NM 87117

Tape springs are of interest to the space structures community because of their high packaging ratios, ability to self-deploy, and high stiffness-to-mass ratios. The current drive to lightweight telescopes has focused mostly on decreasing the mass of the mirrors, yet decreasing the mass of the support structure may also generate significant mass savings. Here the use of carbon-fiber-composite tape springs is examined as a potential support structure of a secondary mirror in a Cassegrain-type telescope configuration. For the tape springs to be useful in this capacity, they must exhibit deployment precision to levels consistent with optical control systems. Deployment repeatability of such structures is investigated through simplified sensing configurations that include a linear structural element and a tripod comprised of carbon-fiber-composite tape springs supporting a simulated secondary mirror. Single tape springs showed deployment repeatability on the order of 100 microns, while the tripod configuration showed deployment repeatability on the order of 50 microns.

I. Introduction

Tape springs are defined as thin-walled, straight strips of material with curved cross-sections, and the most common example of tape springs are carpenters' tape measures.[1] They can be considered thin shells with structural depth determined by the radius and length of the circular-arc-shaped cross-section. Tape springs can be flattened to the shell thickness and folded or rolled. They have the ability to self-deploy, and they are very stiff once straightened. Tape springs offer excellent packaging efficiency in terms of deployed size versus stowed size. Tape springs allow for booms to be stowed and deployed without the use of mechanical joints, making them less complicated, more robust, and less expensive to manufacture than booms with other joint approaches. All of these properties make tape springs attractive for use in space structures, an application for which they have been considered for several years.[2-4]

Using carbon-fiber composites as tape-spring material increases the stiffness-to-mass ratio beyond that of traditional, metal tape springs, allows greater flexibility and customization in their design, and takes advantage of superior thermal expansion properties. Carbon-fiber-composite tape springs have been proposed for use in several space applications, primarily as instrument booms or support trusses.[1-3] The combination of the tape-spring configuration and carbon-fiber-composite material is an optimal solution to the complex problem of selecting space hardware to maximize strength and stiffness while minimizing mass and packaging volume.[4]

Carbon-fiber-composite tape springs have the potential to be widely applicable in satellite systems and are particularly attractive to the space optics community driving for lighter, larger, and therefore more efficient and powerful telescopes. They have not been investigated, however, for optical-level deployment precision. Here, acknowledging the potential for control systems to correct alignment aberrations of several millimeters, optical-level precision refers to a desired repeatability on the order of 100 microns. This paper investigates through experimental

---

[*] Graduate Research Assistant, AIAA Student Member
[††] Graduate Research Assistant, AIAA Student Member
[‡] Research Engineer, AIAA Member
[§] Research Engineer

data the deployment precision of single tape springs in an inherently stable tripod configuration similar in shape to a Ritchey-Chrétien-type Cassegrain telescope. Two types of tape springs were investigated: one comprised solely of carbon-fiber composite and one that incorporates thin metal strips at the hinges to add robustness and increase the packaging ratio.

II. Experimental Setup

Experimental data was recorded for two cases of carbon-fiber-composite tape springs. The first case involved individual springs in a two-dimensional deployment and the second involved three springs in a three-dimensional tripod configuration. The precision and repeatability of the deployments in both cases was measured by On-Trak PSM2 10mm Position Sensing Detectors (PSD's) shown in Figure 1. The PSM2 sensor is a single silicon photodiode 10mm on a side that provides an analog output of location of the centroid of the laser spot incident on its surface to a resolution of 250nm. Lasers were mounted directly to the ends of the tape springs in the two-dimensional (2D) tests and to the simulated secondary mirror in the three-dimensional (3D) tests. Figure 2 shows solid-model representations of the test configurations, which were chosen to gain experience in a traceable geometry with testing the performance of the tape springs both as a single truss element and as a built-up structure. Both tests were conducted while mounted to a large 2.67x2.67x0.61m air-cushioned granite block to isolate the tests from ground vibrations.

Figure 1 – On-Trak position sensing detectors (PSD's) along with notional diagram

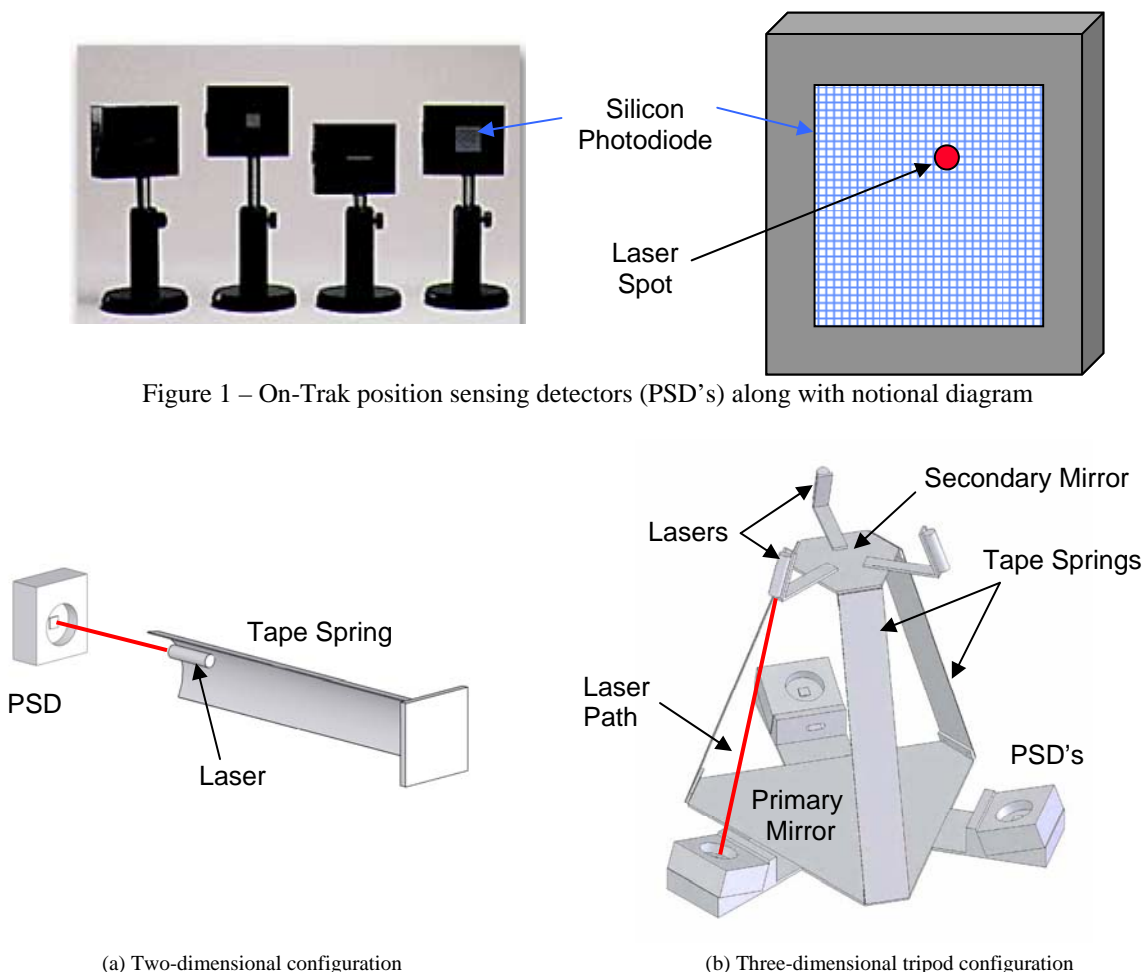(a) Two-dimensional configuration   (b) Three-dimensional tripod configuration

Figure 2 – Experiment configuration for 2D and 3D tests

The tapes springs used the 2D test were selected to match the geometry of those in the 3D test, which was nominally based on the diameter-to-length ratio of a compact Cassegrain space-telescope design. The telescope
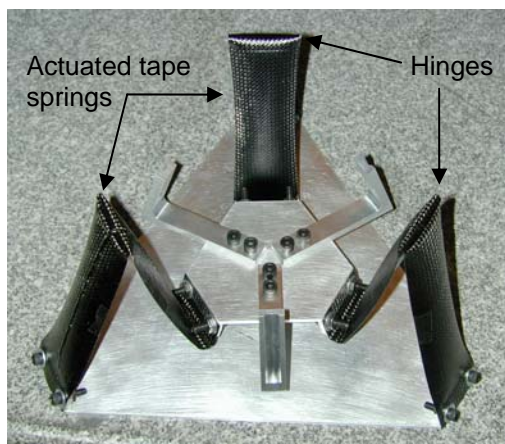
configuration here mimics the shape of a 0.3048*m* (12.00*in*) diameter primary mirror, a 0.1016*m* (4.00*in*) diameter secondary mirror, and a 0.3048*m* standoff distance of the secondary from the primary. In Figure 2(b), the geometries of the triangular plates at the mirror locations, labeled "secondary mirror" and "primary mirror" for simplicity, were determined by inscribing triangles in the 0.3048*m* and 0.1016*m* diameter circles representing the mirrors. This configuration dictated a tape-spring length of 0.3213*m* (12.65*in*). The tape springs, lasers, and sensors are all therefore attached to what would be the outer circumference of the primary or secondary mirrors. The geometry of this 3D test is not ideal as a direct application to telescope; rather, the geometry allows testing of fundamental structural elements with sensor geometry traceable to larger systems. Tape springs of the length, width, and curvature used in the 3D test were also used in the 2D test.

Figure 3 shows images of the 2D and 3D tests. In the 3D testing configuration, the lasers were mechanically mounted on the secondary mirror, but in the 2D tests, they were attached directly to the tape springs. To fix the lasers to the tape spring, each laser was adhered to the tape spring and secured with a pressure fitting of aluminum tape. The aluminum tape was packed around the laser to minimize movement of the laser relative to the tape spring.
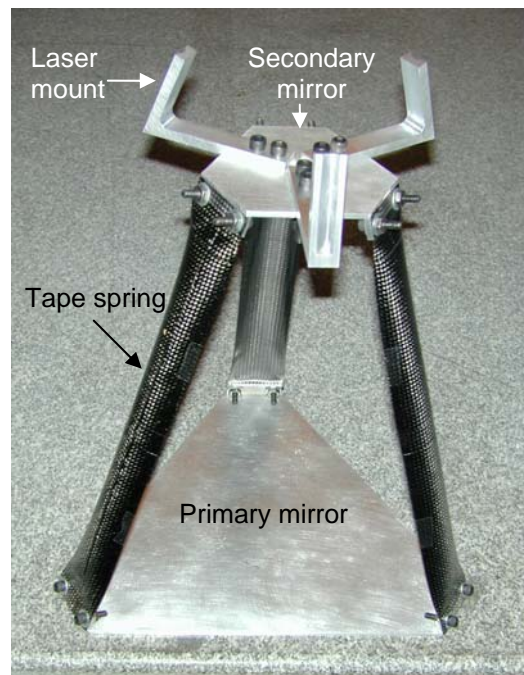
The clamp configuration of Figure 3(a) indicates a difficulty of mounting the tape springs in the 2D configuration. A flat clamp across the entire width of the curved spring was impractical because it would flatten the portion of the spring in the clamp. When part of the spring is flattened, it has little transverse bending stiffness and is therefore too unstable for use in these experimental investigations. Curved clamps presented implementation difficulties. The optimum solution in this case was to clamp a small length of the tape spring over just a portion of the width, as shown in Figure 3(a). No slippage was observed over the several hours of test data taken following each bending event.
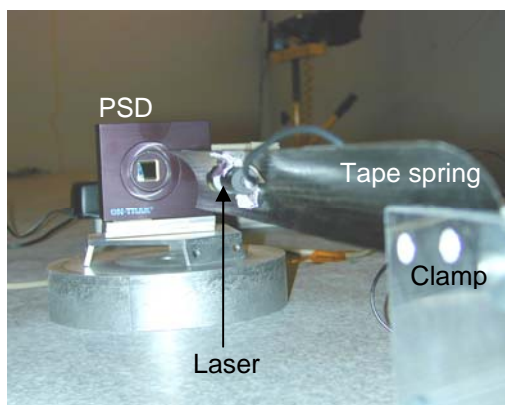
(a) 2D test configuration

(c) 3D deployed test configuration

(b) 3D stowed test configuration

Figure 3 – Test configurations

Tape springs tend to snap back into their original shape after being folded. To reduce the possibility of loosening the laser, the tape springs in the 2D tests were guided slowly back to the deployed configuration by hand and thereby not allowed to snap. In the 3D tests the weight of the secondary mirror was sufficient to prevent the tape springs from returning to a straight (deployed) configuration without assistance. The secondary mirror was therefore also deployed manually to limit any snapping and accompanying shock loads that might alter the laser, spring, and sensor alignment.

III. Tape Spring Design and Manufacturing

Instead of rolling the tape spring along its entire length as in a tape measure – clearly impractical based on the geometry shown in Figures 2(b), 3(b) and 3(c) – the springs used here are manufactured with hinges along their length to allow the tripod structure to be folded down, bringing the secondary mirror directly on top of the primary. The majority of each tape spring is comprised of two plies of woven, +45/-45 IM7-977 carbon-fiber composite with one or more hinges along its length ℓ. Each hinge is 15mm in length, extends the entire width w of the spring, and is comprised of a single ply of IM7. The springs all have a radius of curvature, R, equal to the cylindrical mandrel on which they are cast and subtending 1/3 of the circumference of the circular cross-section ($\theta = 120°$).

When a tape spring bends, the radius of curvature of the bend, r, is equal to the radius R of the spring itself (see Figure 4). The analytic description of $r = R$ can be found in Reference 1. The carbon-fiber composite tolerates fairly high geometric strains, and so the 15mm length (ℓ_h) of the hinge is much less than the radius R of the spring (thus $r << R$). Decreasing r decreases the distance $2r$ between the two folded, flat sections of tape spring and thereby increases the packaging ratio. A decreasing r and $r<<R$ condition also indicate a high-strain condition, however, and associated stress concentrations in the hinge can lead to delamination and eventual failure of the hinge. The stress concentrations on the bent hinge are most severe toward the edges along width w. To maintain a constant r along the entire width w of the hinge and therefore reduce stress concentrations, strips of 1.5mm-wide flat metal ribbon are placed along the outer edges of the tape springs at the hinge locations as shown in Figure 5.

For the hinge on the tape springs to fold, or for any part of the tape spring to roll, it must flatten from its natural curvature R (mathematically, the radius of curvature goes from R to infinity). When part of the spring is flattened, it has little transverse bending stiffness and is easily bent or rolled. In attaching the springs to the metal plates that simulate the primary and secondary mirrors, the springs are flattened at the attachment point. The attachment points are therefore natural hinge locations. Another hinge is added in the middle of the springs, and folded in an opposite direction such that the tripod stows as shown in Figure 3(b). In the 2D tests only one hinge is present in the middle of the springs.
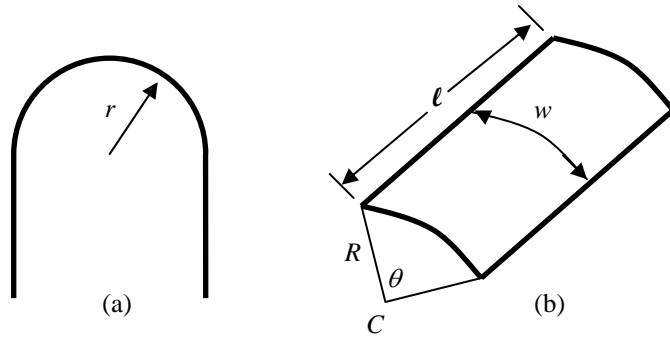

Figure 4 – Geometric variable definitions for the (a) folded and (b) unfolded tape springs
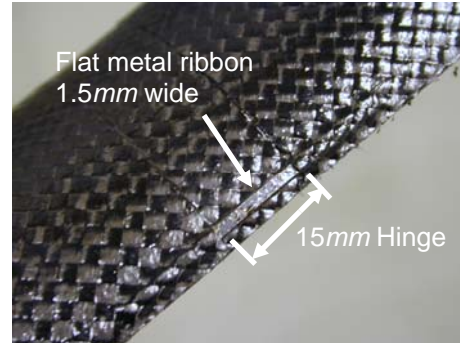

Figure 5 – Tape spring hinge with metal ribbon strip

IV. Sensor Measurements

In the 2D case shown in Figures 2 and 3, the laser was aligned along the central axis of the tape spring and is incident perpendicular to the sensor. Therefore any x or y displacement measured on the sensor related directly to an x or y displacement in the tip of the spring, meaning that configuration was a direct measurement of the position

of the tape spring. The displacement of the tip of the tape spring was determined using right similar triangles as shown in Figure 6.

$$b = ad/c \qquad (1)$$

where a is the distance from the hinge to the tip of the tape spring, b is the displacement of the tip of the tape spring, c is the distance from the hinge to the PSD sensor, d is the displacement measured on the PSD sensor, and all triangles are assumed to be right.
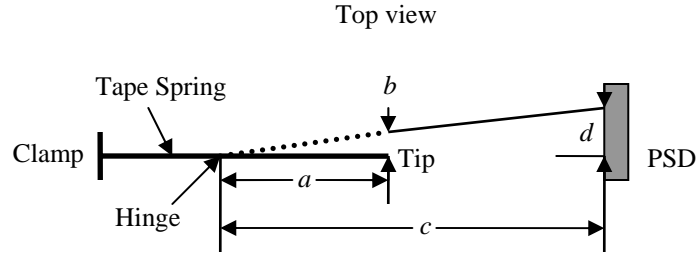
Top view

Figure 6 – Geometric definitions for calculation of tip displacement in 2D tests

In the 3D case the metric of interest is the location of the secondary mirror, not the individual tape springs. Knowledge of six displacement degrees of freedom (DOFs) of the secondary mirror is desirable to assess the precision of the deployment: X and Y (decenter) and Z (piston) positions; and the tip, tilt, and rotational angles (θ_x, θ_y, and θ_z). Several of these DOFs could be measured directly if the sensors were placed level to the secondary mirror and the lasers pointed along the global axes perpendicular to the sensors as in the 2D test setup, e.g. along the y_1 axis of Figure 7(b). To approximate a configuration traceable to a space-based telescope, however, the sensors were placed on the perimeter of the primary mirror. This orientation of sensor placement required transformation equations from sensor displacement data to mirror location data. The derivation of the equations is shown in Appendix A and involves solving for the 3D global-coordinate locations of each of the laser origins as a function of only sensor coordinates. The equations and variables are defined in Equations (2) with reference to Figures 7 and 8 and Appendix A.
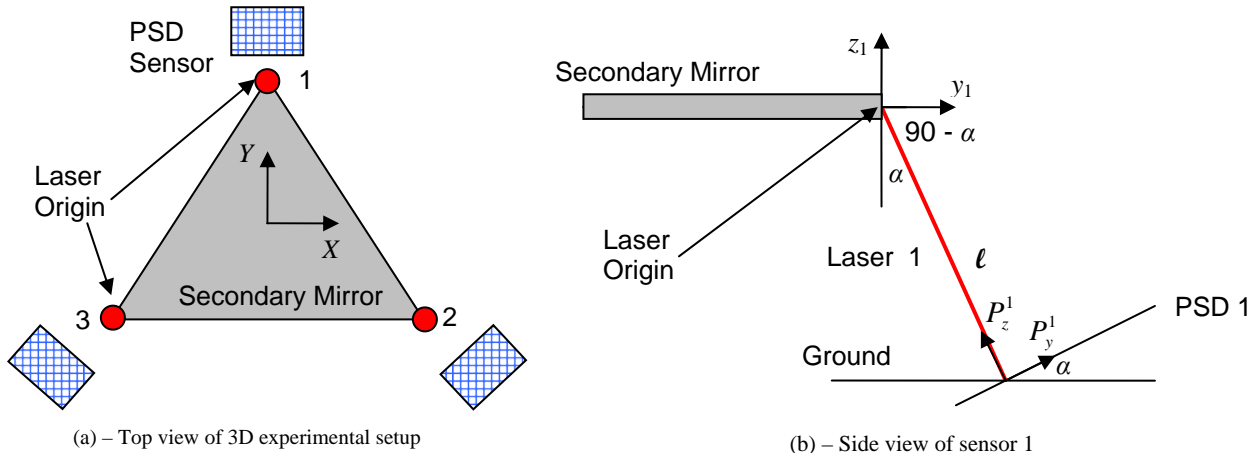

(a) – Top view of 3D experimental setup

(b) – Side view of sensor 1
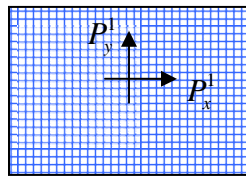
Figure 7 – Relational sensor and laser geometry

Figure 8 – 2D sensor geometry for PSD 1

$$x_1 = P_x^1$$
$$y_1 = P_y^1 \cos(\alpha) - P_z^1 \sin(\alpha) \qquad (2)$$
$$z_1 = P_y^1 \sin(\alpha) + P_z^1 \cos(\alpha)$$

American Institute of Aeronautics and Astronautics

$$x_2 = P_x^2 \cos\phi_1 - P_y^2 \sin\phi_1\cos(\alpha) + P_z^2 \sin\phi_1\sin(\alpha) \qquad x_3 = P_x^3 \cos\psi_1 - P_y^3 \sin\psi_1\cos(\alpha) + P_z^3 \sin\psi_1\sin(\alpha)$$

$$y_2 = P_x^2 \sin\phi_1 + P_y^2 \cos\phi_1\cos(\alpha) - P_z^2 \cos\phi_1\sin(\alpha) \qquad y_3 = P_x^3 \sin\psi_1 + P_y^3 \cos\psi_1\cos(\alpha) - P_z^3 \cos\psi_1\sin(\alpha) \quad \text{(2-cont)}$$

$$z_2 = P_y^2 \sin(\alpha) + P_z^2 \cos(\alpha) \qquad\qquad z_3 = P_y^3 \sin(\alpha) + P_z^3 \cos(\alpha)$$

where P_i^j, $i = \{x, y, z\}$ and $j = \{1, 2, 3\}$, is the displacement defined in Figure 8 on sensor j in direction i, $\{x_k, y_k, z_k\}$, $k = \{1, 2, 3\}$ are the global 3D locations of the laser origin points 1, 2, 3 on the secondary mirror defined in Figure 7, $\phi_1 = -120^\circ$ and $\psi_1 = 120^\circ$ are the rotations about the Z-axis to orient sensors 2 and 3 to the global axes, and α is the angle at which the sensors must be titled above horizontal to create a right angle when the laser strikes the center of the sensor.

The three laser origin points 1, 2, 3 in Figure 7(a) that define the plane of the secondary mirror are used to solve for the centroid position and angular orientation of the secondary mirror. The centroid location allows calculation of the X, Y, and Z displacements as decentering-type and piston-type alignment errors, and the angular orientation directly provides the tip, tilt, and rotational angles. These derivations are also shown in Appendix A.

This approach yields simple, invertable equations yet includes multiple geometric assumptions, and so a simulation was run in which displacements and rotations were applied to the secondary mirror represented by three 3D points corresponding to the laser origin points 1, 2, 3 and vectors representing the laser beams. The locations at which the displaced or rotated laser vectors intersected the sensors were then calculated, and the above Equations (2) and were applied to solve for the three laser origin points on the secondary mirror. Those three three-dimensional points were then used in the equations listed in Appendix A to calculate the six DOFs of the mirror. The results of the study yield an estimation of the error present in the application of Appendix A and Equations (2), where the Input Value was the applied displacement or rotation and the Output Value was the resultant of Equations (2) and Appendix A. For a reasonable range of linear and angular displacements (Input Values) applied individually (0.5 – 5.0mm and 0.1° – 1.0°, respectively), the error between the Output Value result and the Input Value was, in all cases, less than 6%. This error results from the form of Equations (2), which require the local z displacements (P_z^j) on the sensors to exactly calculate the displacements of the laser origin points. The sensors are only capable of measuring local x and y displacements across their surfaces, and therefore in all cases the local z displacement was set to zero ($P_z^j = 0$ for $j = 1,2,3$). The goal of this effort is to demonstrate the order of the shape quality rather than the absolute value, and so this level of error is taken as acceptable.

Because of the size limitations of the sensors and the geometry of the test setup, the maximum X or Y (decenter) displacement of the secondary mirror that could be measured was 5mm, and the maximum Z (piston) displacement was 1.6mm. The maximum tip and tilt about the X and Y axes θ_x and θ_y respectively were 0.9 and 1.0 degrees, and the maximum rotation about the Z axis θ_z was 1.9 degrees.

V. Experimental Data

The 2D data presented here were collected by reading an initial position of the laser attached to the tip of a single tape spring on the PSD, as shown in Figure 3(a), then actuating the hinge and bending the tip of the spring back toward the clamped end. The tip was then guided back to its original position by hand to prevent the spring from snapping into place as discussed above, and the data collection was initiated. The location of the laser on the sensor was recorded every 10 seconds for periods of time ranging from several minutes to several hours. All of the 2D data shown here was taken from multiple bends of two different tape-springs. Figure 9 below shows a sample of the results of the 2D tests of single tape-springs with one hinge in the middle of each spring, one without the strips of metal in the hinge and one with. The data show that the tip position settles over time.

Tables 1(a) and 1(b) show the final displacement data of the tip of the tape spring from its original position. Table 1(a) shows the deployment results for the tape spring without the strip of metal in the 15mm hinge, and Table 1(b) shows the deployment results for the tape springs with the strip of metal in the 15mm hinge.
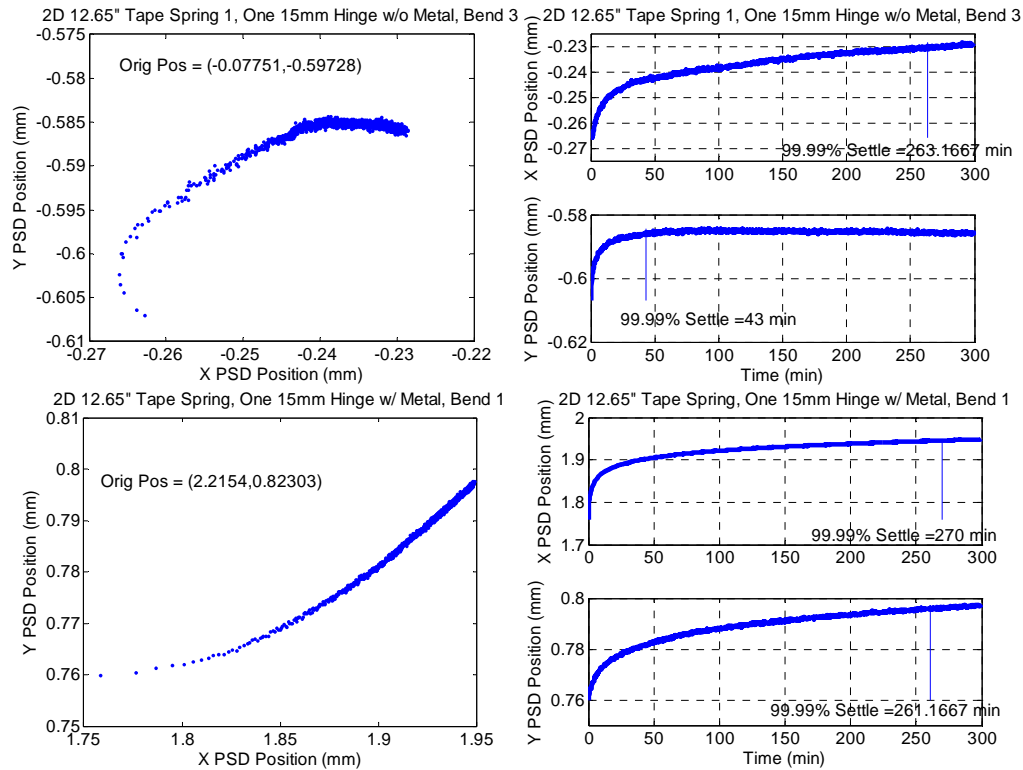
Figure 9 – 2D results for one bend of a single-hinge tape spring without and with the metal strip in the hinge
(top 3 and bottom 3 plots, respectively)

Table 1(a) – 2D displacement data from 12.65*in* spring with one 15*mm* hinge without metal strip

Deployment Count	x Displacement (micron)	y Displacement (micron)	99.99% Settle x (min)	99.99% Settle y (min)
1	745	-299	97	64
2	-155	24	150	117
3	-13	-40	141	127
4	-76	6	263	43
5	-29	35	3.33	0.17
6	-40	3	269	223
Absolute Average	177	68		
Total Displacement		189		

Table 1(b) – 2D displacement data from 12.65*in* spring with one 15*mm* hinge with metal strip

Deployment Count	x Displacement (micron)	y Displacement (micron)	99.99% Settle x (min)	99.99% Settle y (min)
1	-141	-14	270	261
2	50	8	1.33	0.50
3	9	-12	1.17	0.33
4	-15	18		
5	-22	18		
Absolute Average	48	14		
Total Displacement		50		

Tables 1(a) and 1(b) demonstrate that the presence of the metal strip in the hinge of the tape springs leads to a significant improvement in repeatability. Even without the metal strips, however, four of the six bends of the

tape spring yielded final tip displacements from the original position of less than the desired $100\mu m$. The metal strips do, however, achieve a three-fold increase in the precision of the deployments, from $189\mu m$ to $50\mu m$. The "absolute average" value reported in the tables is an average of the absolute displacements from the original position that neglects their signs (directions). The total displacement was calculated as the square root of the sum of the squares of the absolute averages.

Tables 1(a) and 1(b) also report the time required to achieve steady-state displacement positions after the actuation of the tape springs. Several tests were run with varying durations, but in almost all cases a similar steady-state value was observed with consistent recovery of stowage-induced strains. This result was also observed in Reference 5.

It should also be noted that, as seen in Figure 9, the final locations to which the tape springs settled were not the original locations; and in only one of the cases the data trend toward the original location. This disparity likely results not from a permanent elastic deformation in the tape spring but from slippage of the tape spring in the clamp shown in Figure 3(a). Such slippage resulted from the bending of the spring. A more stable method of securing the springs is expected to improve the data quality.

Even with slippage in the clamp, the data in Tables 1(a) and 1(b) indicate that carbon-fiber-composite tape springs are capable of micron-level deployment precision after multiple stow-and-deploy cycles. The data also indicate no significant performance degradation as a function of number of cycles.

The subsequent 3D sets of experimental data checked conclusions of the 2D tests by testing the tape springs in an inherently-stable, deployed-tripod configuration that approximates a compact Cassegrain-type telescope. All of the 3D data presented here were taken by reading initial locations of the lasers on the sensors and then folding the secondary mirror down into the stowed configuration shown in Figure 3(b). The secondary mirror was then slowly raised by hand back up to its starting, deployed position shown in Figure 3(c). The locations of the lasers on the sensors were subsequently recorded every 10 seconds for periods of time ranging from several minutes to several hours. The final locations of the lasers were subtracted from the original locations to yield the sensor displacement results in Tables 2(a) and 2(b). All of the 3D data shown here was taken from multiple deployments of two sets of tape springs. Tables 2(a) and 2(b) show the displacements of the three lasers in the case with one hinge in the middle of each of the three springs; one without the strips of metal in the hinge and one with. P_i^j indicates the displacement in i direction on sensor j, following the naming conventions in Appendix A and Equations (2). The disparity in number of deployments in Tables 2(a) and 2(b) resulted from time constraints.

Table 2(a) – 3D PSD sensor data from tripod setup without metal strips

Deployment Count	P_x^1 (micron)	P_y^1 (micron)	P_x^2 (micron)	P_y^2 (micron)	P_x^3 (micron)	P_y^3 (micron)
1	-155	-32	67	9	134	15
2	27	104	-119	-160	141	28
3	-149	-43	24	76	-183	-22
4	-20	1	-3	-36	-26	17

Table 2(b) – 3D PSD sensor data from tripod setup with metal strips

Deployment Count	P_x^1 (micron)	P_y^1 (micron)	P_x^2 (micron)	P_y^2 (micron)	P_x^3 (micron)	P_y^3 (micron)
1	-45	3	8	78	-64	31
2	188	-58	72	-78	154	-5
3	27	-1	-62	82	115	-27
4	-42	4	-154	196	-336	-8
5	-15	-26	14	7	139	99
6	24	4	2	21	31	12
7	233	-22	-33	-24	-29	3

These data were input into Equations (2) to solve for the locations of the laser origin points on the plane of the secondary mirror, which were then used to solve for the six degree-of-freedom displacements according to Appendix A. The X, Y, Z, θ_x, θ_y, and θ_z quantities reported in Tables 3(a) and 3(b) completely describe the six DOF

movement of the secondary mirror from its original position. The "actual average" values reported are a simple average of the displacement values in the column above each. The "absolute average" values are an average of the displacement magnitudes from the original position. The "total displacement" values are calculated as the square root of the sum of the squares of the absolute averages. The X, Y, and Z displacement data of the secondary mirror are graphed in Figure 10.

Table 3(a) – 3D displacement of secondary mirror from tripod setup without metal strips

Deployment Count	X (micron)	Y (micron)	Z (micron)	θ_x (microrad)	θ_y (microrad)	θ_z (microrad)
1	-87	6	6	5	1	96
2	-46	129	-26	10	41	65
3	4	-82	11	4	21	118
4	-16	-3	-2	2	12	19
Actual Average	-36	12	-3	5	19	74
Absolute Average	38	55	11			
Total Disp		68				

Table 3(b) – 3D displacement of secondary mirror from tripod setup with metal strips

Deployment Count	X (micron)	Y (micron)	Z (micron)	θ_x (microrad)	θ_y (microrad)	θ_z (microrad)
1	7	-37	12	15	10	38
2	5	18	-3	25	16	159
3	30	42	6	7	24	34
4	123	-81	20	25	45	204
5	-56	11	15	7	20	53
6	5	5	3	5	2	22
7	81	-3	0	8	6	110
Actual Average	28	-6	8	13	18	88
Absolute Average	44	28	8			
Total Disp		53				

The results in Tables 3(a) and 3(b) show that the tape springs in the tripod configuration are more stable than they are individually. The average displacements in both hinges without and with metal strips were below $50\mu m$, a three-fold improvement from the single tape spring 2D configuration, and the majority of the tilt and rotation angles are below 100 microradians. Unlike the 2D results, these data show little or no improvement in repeatability from using metal strips in the hinges. All of the data is well within the desired $100\mu m$ bound for optical-level controllability.

Figure 10 shows that most of the final position variability occurs in the XY plane – seen by the random dispersion of data points in that graph versus the other two in which the data points tend to lie along the $Z = 0$ line – indicating there is less error in the Z or piston direction. It also shows that, in all but three of the trials, the displacements after deployment of the tripod were within the $100\mu m$ desired bound (represented by a blue boundary in the figure). The tape-spring tripod is more compliant in the lateral XY plane because the tape springs are much stiffer in axial compression than in lateral cantilever bending, and this increased compliance appears consistent with the wider range of final position.
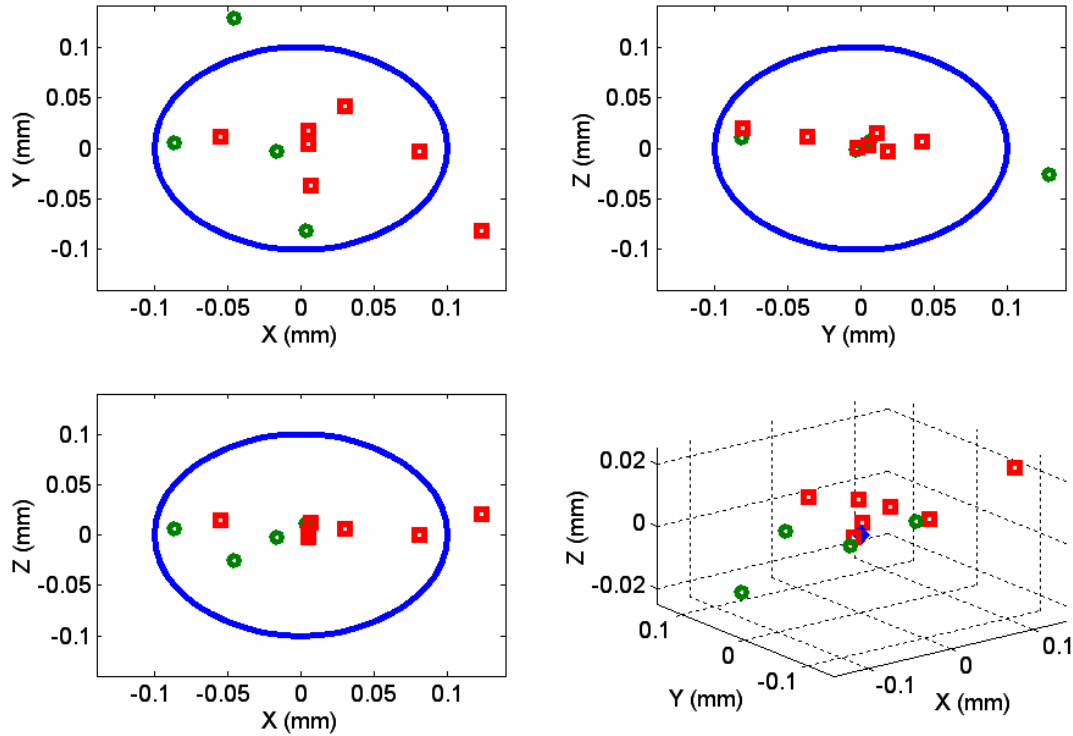
Figure 10 – 3D displacement of secondary mirror from tripod setup without (circle) and with (box) metal strips, large blue oval indicates a $100\mu m$-diameter spherical bound relative to the original location

VI. Summary

Thin walled, straight strips of carbon-fiber-composite weave with curved cross-sections known as tape springs were tested here to determine their utility in optical applications as mirror supports. They were tested in two configurations, as single springs in simple 2D bending tests and in an inherently stable 3D tripod configuration simulating a Ritchey-Chrétien-shaped Cassegrain telescope. A highly accurate sensing system comprised of lasers and photodiode sensors was used (1) to measure the exact location of the tip of the tape spring after bending in the 2D tests and (2) to measure the six displacement degrees of freedom of the secondary mirror after deployment in the 3D tests. Single tape-springs measured in two dimensions were found to return to within $100\mu m$ of their original positions on average. There was also no significant degradation in precision as a function of number of bends. The stable 3D tripod configuration showed a more accurate deployment precision than the individual springs. The average displacement of the 3D deployments was approximately $50\mu m$, again well within the desired optical precision levels of about $100\mu m$.

References

[1]Yee, J.C.H., Soykasap, O, and S. Pellegrino, "Carbon Fibre Reinforced Plastic Tape Springs," AIAA-2004-1819.
[2]G. Pica, et. al., "High Resolution Deployable Telescope for Satellite Application," Proceedings of SPIE Volume: 5234, p 531-538, Feb. 2004.
[3]Ng, T.T., and T.W. Murphey, "A Novel Deployable Boom with Flexible Hinges," AIAA-2005-2197.

[4]Murphey, T.W., "A Material Structural Performance Index for Strain Based Deployable Trusses," 45th AIAA Structures, Structural Dynamics, and Materials Conference, Palm Springs, CA, April 2004, AIAA-2004-1656.

[5]Domber, J.L, Hinkle, J.D., Peterson, L.D., and P.A. Warren, "Dimensional Repeatability of an Elastically Folded Composite Hinge for Deployed Spacecraft Optics," Journal of Spacecraft and Rockets, Vol. 39, No. 5, Sept.-Oct. 2002, p 646-652.

Appendix A

The objective is to solve for the global X,Y,Z-direction displacements on the secondary mirror as a function of displacements on the PSD sensors. The geometry of the secondary mirror and sensor is provided in Figure 7, and that of the PSD sensor in Figure 8. The equations below are derived based on the assumption that the displacement vectors from the original pre-stowage laser spots to the new post-deployment laser spots measured by the PSD sensors in the local coordinate systems are identical to the corresponding 3D displacement vectors of the laser origin points.

For sensor #1 the PSD displacement vector components in the local PSD coordinate system are $\{P_x^1, P_y^1, P_z^1\}$, and laser origin point displacement vector components in the global coordinate system are $\{x_1, y_1, z_1\}$. The two coordinate systems are related through a single coordinate rotation $\phi = \alpha$ about the local x-axis. Assuming the two vectors are equal, the equation below shows the PSD displacement vector as viewed from the global coordinate system.

$$\begin{Bmatrix} x_1 \\ y_1 \\ z_1 \end{Bmatrix} = \begin{bmatrix} 1 & 0 & 0 \\ 0 & \cos(\alpha) & -\sin(\alpha) \\ 0 & \sin(\alpha) & \cos(\alpha) \end{bmatrix} \begin{Bmatrix} P_x^1 \\ P_y^1 \\ P_z^1 \end{Bmatrix} \tag{A.1}$$

For sensor #2 the PSD displacement vector components in the local PSD coordinate system are $\{P_x^2, P_y^2, P_z^2\}$, and laser origin point displacement vector components in the global coordinate system are $\{x_2, y_2, z_2\}$. The two coordinate systems are related through a series of rotations first about the global Z-axis $\phi_1 = -120^\circ$ and then $\phi_2 = \alpha$ about the local x-axis. Assuming the two vectors are equal, Equation A.4 shows the PSD displacement vector as viewed from the global coordinate system.

$$\begin{Bmatrix} a_1 \\ a_2 \\ a_3 \end{Bmatrix} = \begin{bmatrix} \cos(\phi_1) & \sin(\phi_1) & 0 \\ -\sin(\phi_1) & \cos(\phi_1) & 0 \\ 0 & 0 & 1 \end{bmatrix} \begin{Bmatrix} x_2 \\ y_2 \\ z_2 \end{Bmatrix} \tag{A.2}$$

$$\begin{Bmatrix} P_x^2 \\ P_y^2 \\ P_z^2 \end{Bmatrix} = \begin{bmatrix} 1 & 0 & 0 \\ 0 & \cos(\phi_2) & \sin(\phi_2) \\ 0 & -\sin(\phi_2) & \cos(\phi_2) \end{bmatrix} \begin{Bmatrix} a_1 \\ a_2 \\ a_3 \end{Bmatrix} \tag{A.3}$$

With the substitution $\phi_2 = \alpha$ and matrix multiplication,

$$\begin{Bmatrix} x_2 \\ y_2 \\ z_2 \end{Bmatrix} = \begin{bmatrix} \cos\phi_1 & -\sin\phi_1\cos\alpha & \sin\phi_1\sin\alpha \\ \sin\phi_1 & \cos\phi_1\cos\alpha & -\cos\phi_1\sin\alpha \\ 0 & \sin\alpha & \cos\alpha \end{bmatrix} \begin{Bmatrix} P_x^2 \\ P_y^2 \\ P_z^2 \end{Bmatrix} \tag{A.4}$$

For sensor #3 the PSD displacement vector components in the local PSD coordinate system are $\{P_x^3, P_y^3, P_z^3\}$, and laser origin point displacement vector components in the global coordinate system are $\{x_3, y_3, z_3\}$. The two coordinate systems are related through a series of rotations first about the global Z-axis $\psi_1 = 120^\circ$ and then $\psi_2 = \alpha$ about the local x-axis. Assuming the two vectors are equal, Equation A.5 shows the PSD displacement vector as viewed from the global coordinate system. The derivation is identical to that for sensor #2.

$$\begin{Bmatrix} x_3 \\ y_3 \\ z_3 \end{Bmatrix} = \begin{bmatrix} \cos\psi_1 & -\sin\psi_1\cos\alpha & \sin\psi_1\sin\alpha \\ \sin\psi_1 & \cos\psi_1\cos\alpha & -\cos\psi_1\sin\alpha \\ 0 & \sin\alpha & \cos\alpha \end{bmatrix} \begin{Bmatrix} P_x^3 \\ P_y^3 \\ P_z^3 \end{Bmatrix} \tag{A.5}$$

The laser origin point displacement vectors $\{x_1, y_1, z_1\}$, $\{x_2, y_2, z_2\}$, and $\{x_3, y_3, z_3\}$ must then applied directly to the original pre-stowage laser origin point locations in global 3D space, resulting in the new post-deployment locations of the laser origin points. However, equations A.1, A.4, and A.5 can be modified from simple coordinate rotations to solve directly for the laser origin points by adding the vector $\{0, 0, \ell\}$, as shown below. This indicates that the sensors are actually a distance ℓ from the laser origin points, as shown in Figure 7.

$$\begin{Bmatrix} x_1 \\ y_1 \\ z_1 \end{Bmatrix} = \begin{bmatrix} 1 & 0 & 0 \\ 0 & \cos(\alpha) & -\sin(\alpha) \\ 0 & \sin(\alpha) & \cos(\alpha) \end{bmatrix} \left(\begin{Bmatrix} P_x^1 \\ P_y^1 \\ P_z^1 \end{Bmatrix} + \begin{Bmatrix} 0 \\ 0 \\ \ell \end{Bmatrix} \right) \tag{A.6}$$

$$\begin{Bmatrix} x_2 \\ y_2 \\ z_2 \end{Bmatrix} = \begin{bmatrix} \cos\phi_1 & -\sin\phi_1\cos\alpha & \sin\phi_1\sin\alpha \\ \sin\phi_1 & \cos\phi_1\cos\alpha & -\cos\phi_1\sin\alpha \\ 0 & \sin\alpha & \cos\alpha \end{bmatrix} \left(\begin{Bmatrix} P_x^2 \\ P_y^2 \\ P_z^2 \end{Bmatrix} + \begin{Bmatrix} 0 \\ 0 \\ \ell \end{Bmatrix} \right) \tag{A.7}$$

$$\begin{Bmatrix} x_3 \\ y_3 \\ z_3 \end{Bmatrix} = \begin{bmatrix} \cos\psi_1 & -\sin\psi_1\cos\alpha & \sin\psi_1\sin\alpha \\ \sin\psi_1 & \cos\psi_1\cos\alpha & -\cos\psi_1\sin\alpha \\ 0 & \sin\alpha & \cos\alpha \end{bmatrix} \left(\begin{Bmatrix} P_x^3 \\ P_y^3 \\ P_z^3 \end{Bmatrix} + \begin{Bmatrix} 0 \\ 0 \\ \ell \end{Bmatrix} \right) \tag{A.8}$$

Note that the quantities P_z^j for j = {1, 2, 3} are not measurable but are assumed to be small. With the addition to the large quantity ℓ, however, the small quantities P_z^j are approximated as zero.

With the new post-deployment $\{x,y,z\}$ locations of the laser origin points, the next step is to calculate the position of the secondary mirror using the centroid and rotation variables below.

$$\text{Secondary Mirror Centroid} = \begin{Bmatrix} X \\ Y \\ Z \end{Bmatrix} \qquad\qquad \text{Secondary Mirror Rotations} = \begin{Bmatrix} \theta_x \\ \theta_y \\ \theta_z \end{Bmatrix} = \begin{Bmatrix} \theta_{tip} \\ \theta_{tilt} \\ \theta_{rotation} \end{Bmatrix}$$

The centroid is a simple average due to the symmetric shape of the "secondary mirror",

$$\begin{Bmatrix} X \\ Y \\ Z \end{Bmatrix} = \begin{Bmatrix} (x_1 + x_2 + x_3)/3 \\ (y_1 + y_2 + y_3)/3 \\ (z_1 + z_2 + z_3)/3 \end{Bmatrix} \tag{A.9}$$

and the change in position of the secondary mirror is taken as the difference between the new post-deployment measurement and the original pre-stowage measurement.

To find rotations, orthogonal unit vectors $\hat{C} = \{\hat{C}_1, \hat{C}_2, \hat{C}_3\}$ are introduced through intermediate vectors $\{\vec{b}_{32}, \vec{b}_{31}\}$ defined below.

$$\vec{b}_{32} = \begin{Bmatrix} x_2 - x_3 \\ y_2 - y_3 \\ z_2 - z_3 \end{Bmatrix} \qquad\qquad \vec{b}_{31} = \begin{Bmatrix} x_1 - x_3 \\ y_1 - y_3 \\ z_1 - z_3 \end{Bmatrix} \tag{A.10}$$

$$\hat{C}_1 = \frac{\vec{b}_{32}}{\left\| \vec{b}_{32} \right\|} = \left\{ \begin{matrix} x_2 - x_3 \\ y_2 - y_3 \\ z_2 - z_3 \end{matrix} \right\} / \sqrt{(x_2 - x_3)^2 + (y_2 - y_3)^2 + (z_2 - z_3)^2}$$

$$\hat{C}_3 = \frac{\vec{b}_{32} \times \vec{b}_{31}}{\left\| \vec{b}_{32} \times \vec{b}_{31} \right\|}$$

$$\hat{C}_2 = \hat{C}_3 \times \hat{C}_1$$

(A.11)

θ_x, θ_y, and θ_z are defined through an assumption of small rotations between original-position basis vectors $\hat{C}^0$ to the deployed-position basis vectors $\hat{C}^{new}$. A graphical representation of the angles is shown in Figure A.1.

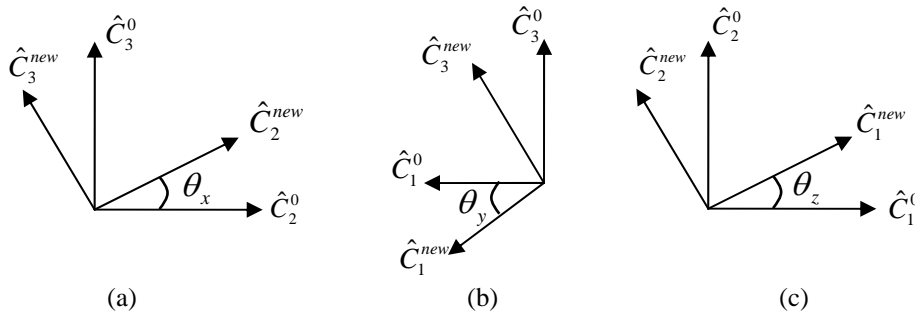|		
(a)	(b)	(c)

Figure A.1 – Rotational displacements are defined through a small-displacement assumption and the change in basis vectors representing the secondary mirror orientation.

The projection in the Y-Z plane leads to the definition for rotation about the X-axis, θ_x, from either the change in $\hat{C}_2$ axis or change in $\hat{C}_3$. The average value is used here..

$$\theta_x = \left[\arccos\left(\frac{\hat{C}_2^0 \cdot \hat{C}_2^{new}}{\left\| \hat{C}_2^0 \right\| \left\| \hat{C}_2^{new} \right\|} \right) + \arccos\left(\frac{\hat{C}_3^0 \cdot \hat{C}_3^{new}}{\left\| \hat{C}_3^0 \right\| \left\| \hat{C}_3^{new} \right\|} \right) \right] / 2$$

(A.12)

The same formulation is applied to generate θ_y and θ_z defined in Figure A.1 above from the two basis-vector sets $\hat{C}^0$ and $\hat{C}^{new}$.

In summary, Equations A.1, A.4, and A.5 are used with PSD data for x- and y-directions and zero values for the z-direction. The corner-point locations of the secondary mirror are then used in Equations A.9-A.12 to estimate the position of the secondary mirror.